Applied Physics Letters

Violet phosphorus surface chemical degradation in comparison to black phosphorus

Cite as: Appl. Phys. Lett. **118**, 163105 (2021); https://doi.org/10.1063/5.0045090
Submitted: 22 January 2021 . Accepted: 05 April 2021 . Published Online: 22 April 2021

Alireza Fali, Michael Snure, and Yohannes Abate

Applied Physics Letters ARTICLE scitation.org/journal/apl

Violet phosphorus surface chemical degradation in comparison to black phosphorus

Cite as: Appl. Phys. Lett. **118**, 163105 (2021); doi: 10.1063/5.0045090
Submitted: 22 January 2021 · Accepted: 5 April 2021 ·
Published Online: 22 April 2021

View Online Export Citation CrossMark

Alireza Fali,[1] Michael Snure,[2] and Yohannes Abate[1,a)]

AFFILIATIONS

[1]Department of Physics and Astronomy, University of Georgia, Athens, Georgia 30602, USA
[2]Air Force Research Laboratory, Sensors Directorate, Wright Patterson Air Force Base, Ohio 45433, USA

[a)]Author to whom correspondence should be addressed: yohannes.abate@uga.edu

ABSTRACT

Bulk growth methods have made it possible to synthesize several allotropes of phosphorus such as black, white, red, and violet phosphorus. However, unlike exfoliated black phosphorus (BP), which has been extensively studied, much of the optoelectronic properties and stability of the other allotropes have yet to be comprehensively investigated. Here, we study the chemical degradation of exfoliated violet phosphorus (VP) in comparison to BP under ambient conditions using nanoscale infrared spectroscopy and imaging. We identify oxidized phosphorus species that result from chemical reaction processes on the surfaces of these phosphorus allotropes. We have found that VP exhibits a noticeably different and slower degradation process when compared to BP, establishing it as the more stable of the two allotropes. A better understanding of the stability of VP could lead to the further fundamental study of its monolayer form for potential future applications.

Black phosphorus (BP) has been synthesized for over 100 years,[1] but the interest in BP in contemporary materials research accelerated due to its exfoliable nature, which makes it a member of the van der Waals materials (vdW) family. BP's orthorhombic crystal structure with a space group Cmca is an anisotropic in-plane displaying two independent in-plane components of the dielectric tensor that are different from each other.[2] The bandgap of BP is tunable, direct, and narrow, making it suitable for nanoelectronics and nanophotonics applications.[3] It also displays thickness dependent on/off current ratio in the range of 10^3–10^5 and decent saturation characteristics that make it a candidate for digital logic applications in thin film electronics as well as flexible electronics.[4] In addition to BP, there are two other layered allotropes of phosphorus: violet and blue. These allotropes, which are all p-type, have distinct structures and band gaps ranging from narrow BP (0.3 eV)[5] to mid bandgap violet phosphorus (VP) (1.7 eV)[6] and blue phosphorus (2 eV).[7]

vdW heterostructures based on BP have presented great opportunities for application in nanoelectronics.[8] For instance, the Schottky barrier height and doping of BP can be controlled by electrostatic gating in graphene/BP heterostructures, and BP/MoS_2 p–n junctions show strong gate-tunable current-rectifying I–V characteristics.[9] With multiple layered allotropes, phosphorus offers the unique opportunity to form 2D heterostructures using this single element. Recently, the work function and bandgap of VP were investigated, showing an increasing work function from 4.79 to 5.17 eV with decreasing number of layers from bulk, while the bandgap increases from 1.7 to ∼2eV.[6] Coupled with the thickness tunable bandgap (0.3–1.5 eV)[10] and work function (4.56–5.17 eV) of BP, this suggests both type I and type II heterostructures may be possible with BP/VP via thickness tuning. Experimentally, heterostructures of BP/VP have been observed during chemical vapor transport (CVT) synthesis[11] and by annealing BP flakes in tertiarybutylphosphine (TBP).

Oxidation and degradation of BP films remain a considerable challenge affecting charge impurities in the surface and substrate environment resulting in scattering centers that can significantly reduce the carrier mobility. Researchers have been endeavoring to accelerate the use of BP by overcoming the formidable challenge of preserving thin BP from oxidation.[4] In addition to ongoing efforts to find ways to stabilize BP, the search for other more stable phosphorus allotropes and phosphorous-based heterostructures is under way. A recent example is the successful exfoliation of violet phosphorene from bulk VP crystals grown by CVT.[6,12] Although BP has been largely reported as the most stable phosphorus allotrope, Zhang *et al.*[6] recently reported VP to be thermally stable to 512 °C compared to 460 °C for BP. However, much of VP's ambient stability in comparison to BP remains unknown.

In this work, we investigate the surface chemical degradation of exfoliated VP flakes and compare its surface oxidation with BP

samples under ambient conditions over time. We performed nanoscale infrared spectroscopy (nano-FTIR) in the frequency range of 800–1500 cm^{-1} by mapping the local ambient spectral changes at nanometer spatial resolution. The nano-FTIR spectra taken on VP and BP flakes show broad spectra arising from several overlapping vibrational modes from phosphoric species produced due to degradation. The topography and surface degradation evolution of VP flakes are different from surface and height changes observed on BP flakes. VP shows more stability than BP as revealed by the surface topographic and dielectric changes on the surface over time. In BP, the degradation begins at random locations as bubbles then evolves abruptly over a large area via the connection of local bubbles toward saturation following a sigmoid growth curve. The degradation effects we observe in VP through topography and nano-FTIR spectra are noticeably different from BP, which highlight differences in the degradation process of these two phosphorus allotropes. Additionally, we identify the formation of VP on BPs flakes during annealing under TBP, demonstrating the possibility of forming VP/BP heterostructures. The 2D phosphorous semiconductor allotrope family spans a wide range of optoelectronic properties; their combination would allow the unique opportunity to build a single-element vdW heterostructure.

Flakes of BP and VP were transferred from bulk sources onto SiO_2/Si for characterization. Bulk BP produced by CVT was purchased from 2D semiconductors, and the bulk VP was produced in-house by chemical vapor deposition (CVD). For VP synthesis, a quartz crucible was loaded into the CVD chamber filled with 0.1g SnI_4 and 0.1g Sn metal and covered with a sapphire wafer, evacuated, and filled with N_2:H_2 (95%:5%) to a pressure of 700 Torr. Then, the reactor was heated to 600 °C, and the phosphorus source TBP was flowed at a flow rate of 40 sccm with 160 sccm of N_2:H_2 for 30 min. The reactor was then cooled to 400 °C under flowing TBP and N_2:H_2. After reaching 400 °C, TBP was turned off and the reactor cooled to room temperature. Small flakes of VP that formed on the edges of the crucible and sapphire wafer were transferred to SiO_2/Si for characterization using a polydimethylsiloxane (PDMS) stamp. For VP/BP samples, BP flakes were exfoliated onto a SiO_2/Si substrate, loaded into the CVD chamber, evacuated, and filled with N_2:H_2 to a pressure of 700 Torr. The reactor was then heated to 450 °C under flowing N_2:H_2. After reaching temperature, TBP was introduced at a flow rate of 40 sccm for 10 min and then cooled to 400 °C before turning off TBP and cooling to room temperature.

Raman spectra comparing exfoliated BP and VP flakes captured using a Renishaw inVia system using a 488 nm excitation source under a backscattering geometry are shown in Fig. 1. BP spectrum clearly show the three distinct A_g^1, E_{2g}, and A_g^2 Raman modes at 365, 425, and 450 cm^{-1} [Fig. 1(a)]. In contrast, the VP spectrum [Fig. 1(b)] reveals numerous peaks in the range of 100–300 and 350 to <500 cm^{-1} consistent with recent reports on bulk VP synthesis.[6,11,12] Compared with the orthorhombic structure of BP, VP's monoclinic structure is quite complex consisting of layers of perpendicular phosphorus tube structures covalently linked with space group P2/n (13)[6] [Fig. 1(c)]. The VP Raman spectrum can be broken down into three regions based on bond distortions: high due to stretching and bending (350 to <500 cm^{-1}) modes, mid due to angle distortions (175–300 cm^{-1}), and low frequency due to rotational deformations (<175 cm^{-1}).[13] The distinct crystal and band structures of BP and VP offer the possibility to form unique single element van der Waals heterostructures by

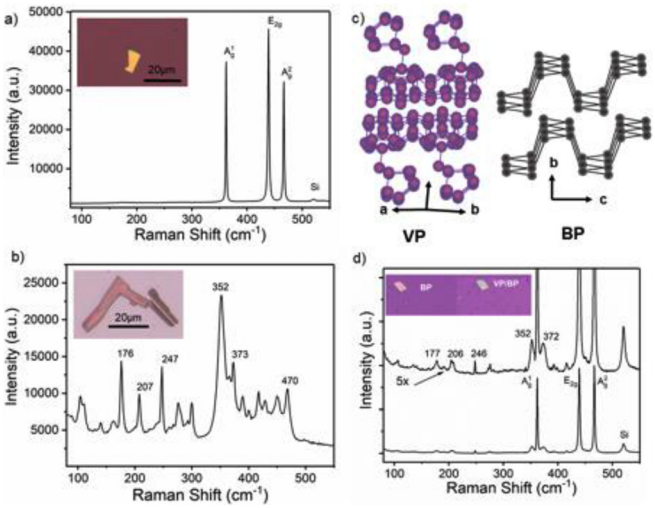

FIG. 1. Raman characterization of BP, VP, and heterostructure. (a) Raman spectrum of a ~65 nm-thick BP flake on SiO_2/Si substrate. Inset shows optical image of BP flake. (b) Raman spectrum of a ~430 nm-thick VP flake on SiO_2/Si. Inset shows optical image of as-grown VP flakes. (c) Schematic comparing the structures of VP and BP. (d) Raman spectra of VP/BP heterostructure. Top curve is magnified by 5× to show VP portion of the spectrum. Inset shows optical image of transferred BP flake and the same flake after the formation of VP/BP.

combining narrow band BP (0.3 eV) with mid band VP (1.7 eV).[6] Figure 1(d) shows Raman spectra and optical images of a ~42 nm BP flake on SiO_2/Si after annealing under TBP at 450 °C. Optical images show the flake remains intact, while Raman shows a spectrum with both BP and VP Raman modes demonstrating the possibility of producing such heterostructures. Similarly, heterostructures have also been reported during CVT synthesis.[11,12]

Topographic and near-field broadband IR optical images and nanoscale infrared spectra were acquired using a commercial nano-FTIR setup (neaspec.com), which is extensively described in previous publications.[14–16] Briefly, it is based on a tapping mode AFM with a cantilevered metal-coated tip that oscillates at a resonance frequency of $\Omega \sim 280$ kHz and a tapping amplitude of ~50 nm. A coherent broadband infrared beam in the frequency range 700–2100 cm^{-1} is focused by a parabolic mirror to the tip. The backscattered near-field light from the tip-sample junction is detected via mixing with an asymmetric Fourier transform Michelson interferometer, enabling detection of the amplitude $s(\omega)$ and phase $\varphi(\omega)$ spectra of the backscattered light. To extract background-free local near-fields, the detector signal is demodulated at a higher harmonic $n\Omega$ of the tip mechanical resonance frequency Ω. Normalized amplitude $[s_n(\text{sample})/s_n(\text{reference})]$ and phase $[\varphi_n(\text{sample})-\varphi_n(\text{reference})]$ IR near-field spectra are acquired by first taking reference spectrum on a reference area (silicon is used in these experiments), followed by taking spectra at desired positions on the sample.

We studied the surface chemical modification of phosphorus allotropes (VP and BP) under ambient conditions over time by collecting local spectral changes using nano-FTIR spectroscopy in the frequency range 800–1500 cm^{-1}. The normalized second harmonic phase spectra of an exfoliated 430 nm-thick VP sample and a 27 nm-thick BP sample taken over several days are shown in

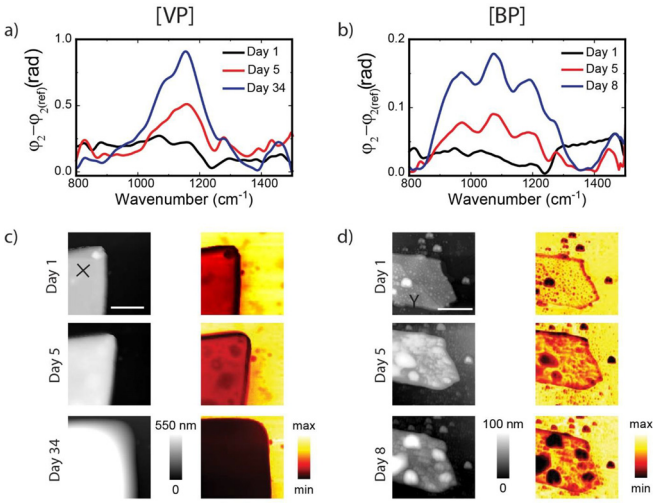

FIG. 2. Nano-FTIR phase spectra, topography, and near-field amplitude images of VP and BP. (a) and (b) Experimental nano-FTIR phase spectra of VP and BP, respectively, under ambient conditions over time taken at positions marked X and Y in (c) and (d) topographic images, respectively. (c) and (d) Topographic and second harmonic broadband IR near-field amplitude images of VP and BP, respectively, taken at different days. Scale bars shown in topographic (day 1) images in (c) and (d) represent 2 μm.

Figs. 2(a) and 2(b), respectively. Silicon substrate is used as a reference area to normalize the phase spectra. The phase spectra of VP [taken at the position marked X in Fig. 2(c) day 1] show mainly a broad peak centered around ~1150 cm^{-1} with a shoulder around 1080 cm^{-1} that increase in intensity with time. The phase spectra of BP [taken at the position marked Y in Fig. 2(d) day 1] show a more complex spectra with 3 resolved peaks on top of a broad background in the range 850–1300 cm^{-1} that increase in intensity with time (going from day 1 to day 8).

The mechanism of BP degradation is complex and has been reviewed extensively.[4] The unstable bonding structure arises from the free electron lone pairs of phosphorus atoms, making BP susceptible to degradation at a rate that depends on oxygen and water concentration, light intensity, and energy gap. The degradation of the surface results in several phosphorus oxides (P_xO_y) and phosphoric acid species that exhibit stretch modes in the frequency range spanning 800 cm^{-1}–1300 cm^{-1}. This is clearly captured in the nano-FTIR spectra taken on VP and BP flakes shown in Fig. 2. The main peaks in these spectra are broad due to a combination of many overlapping modes arising from several phosphoric species. The spectral intensity in both BP and VP increases over time due to increased formation of surface phosphorus oxide products. Oxygen plays a major role in the degradation mechanism by destroying BP's structure via the formation of P–O–P bonds; as such, the dominant vibrational peaks are related to P–O stretch modes. The range 870–950 cm^{-1} has been assigned to P–O stretching vibrations in Ref. 17, whereas symmetric phosphate (PO_2-) stretching vibrations are centered at 1080 cm^{-1},[18] and the range 1180–1250 cm^{-1} is assigned as P = O stretch modes.[19] Similar to BP, oxygen is expected to play a major role in the degradation mechanism of VP, and vibrational peak assignments should be similar. However, the strong presence of P–O stretch modes in BP, which is not observed in VP, suggests reduced oxygen insertion in VP leading to slower degradation. This is also reflected in the thickness and permittivity changes of these flakes as shown in the topographic and near-field amplitude images (Fig. 3) discussed below.

Topographic and second harmonic broadband IR near-field amplitude images of the VP flake shown in Fig. 2(c) reveal how degradation evolves in an ambient environment over the course of several days. Comparing the topography of day 1 and day 34 shows that it has uniformly increased in thickness to 1135 nm over the measured area. On the other hand, the topographic change for the BP flake shown in Fig. 2(d) is different increasing from 27 nm up to 81 nm in certain areas, which begins with randomly scattered bubbles on the surface because of the degradation. The second harmonic broadband IR near-field amplitude image of VP in Fig. 2(c) reveals changes in contrast between day 1 and day 5 with the appearance of dark spots. By day 34, the whole flake appears uniformly dark with respect to the substrate. This is because the near-field infrared photons' probe changes in the permittivity of the sample, where a dark signal (with respect to the substrate) implies the degradation of the VP flake. Comparing this degradation behavior with BP, a similar appearance of dark spots is observed but with a different trend in how the topography and amplitude contrasts change with time. In BP, these changes start as small bubbles and grow bigger. The changes in topography and near-field amplitude signal are analyzed below.

Topographic and IR near-field amplitude spectra analysis shown in Fig. 3 reveal the degradation of VP and BP surfaces in an ambient environment over the course of several days. The topography of the VP flake changes over time in a way that is noticeably different from surface and height changes observed on BP flakes. First, VP shows more stability than BP as revealed by the topographic and dielectric changes on the surface. Second, VP degradation begins at random locations as bubbles similar to BP. However, in VP, degradation evolution is abrupt and large scale, unlike BP, which evolves via connection of local bubbles toward saturation following a sigmoid growth curve (see Refs. 20 and 21 also for BP degradation study). In both VP and BP surfaces, topographically higher nano-islands appear darker than the substrate in the amplitude images. Such a negative contrast in the broadband IR near-field amplitude images is due to the small dielectric constant of the degraded islands compared to the undegraded areas, which are identified as phosphorus oxide species in the phase spectra shown in Fig. 2.

We extracted topographic geometric changes (thickness and area) and the corresponding near-field amplitude spectra over time in VP and BP flakes and compare them with an analytical model. In Figs. 3(a) and 3(b), we show plots of the normalized change in topographic height percentage ($\frac{\Delta t}{t_i}$ %) over time for VP flake at point X [in Fig. 2(c)] and BP flake at point Y [in Fig. 2(d)], respectively. We note that spots X and Y are chosen as exemplary/arbitrary points, respectively. Here, t_i is the initial thickness of the flake at the start of the experiment (day 1) and Δt is the topographic thickness change ($t_n - t_i$, where t_n is the height on the day measured). From linear fits (red line) to experimental data in Figs. 3(a) and 3(b), the slope of the normalized change in topographic height percentage in BP ($m_{BP} = 2.79$/day) is a factor of ~9 larger than that of slope of VP ($m_{VP} = 25$/day). The slope comparison shows that the change in flake heights increases linearly for both VP and BP samples with time as they degrade; however, BP shows a large topographic height changeover the same time period

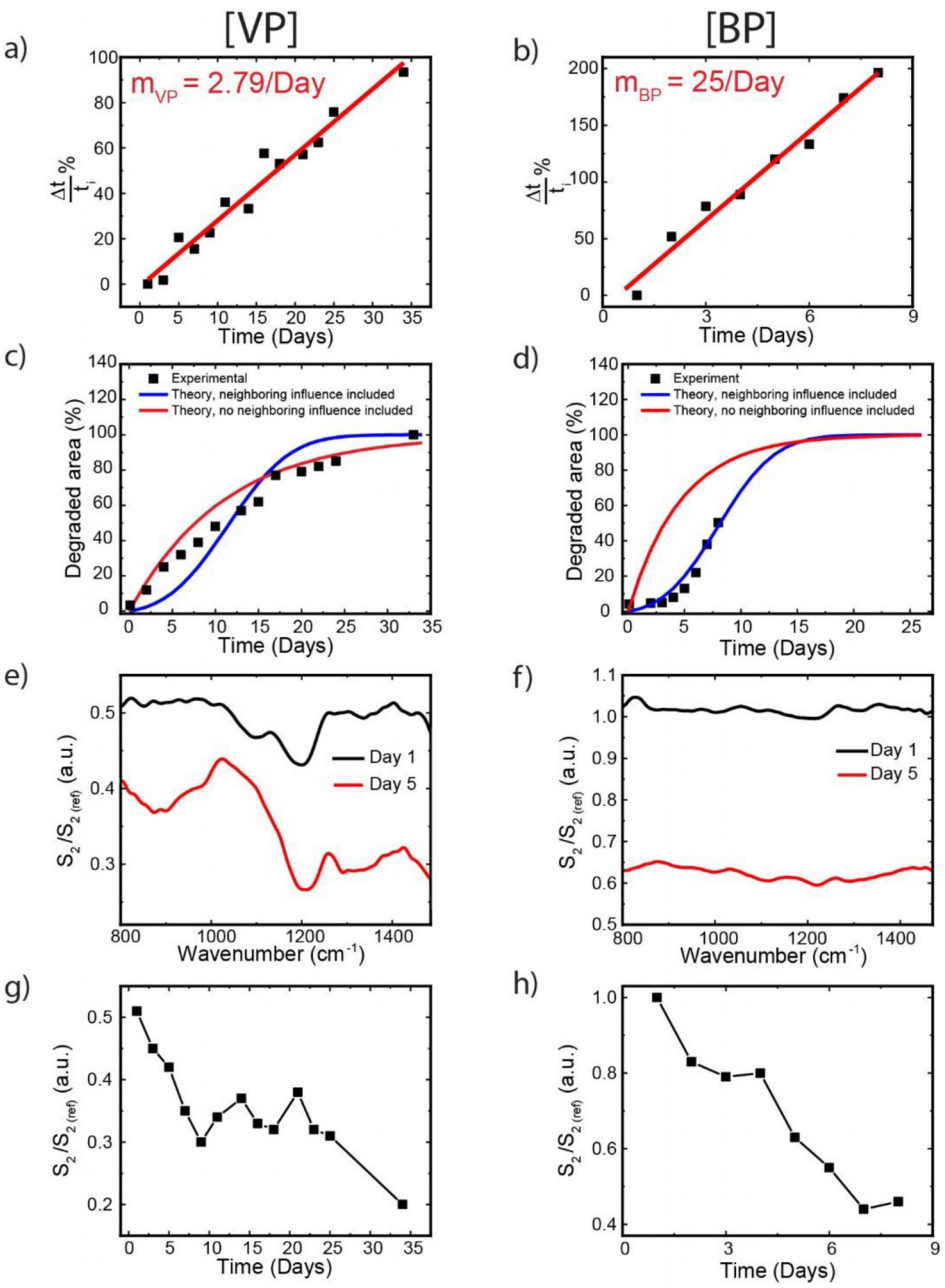

FIG. 3. Normalize change in topographic height percentage ($\frac{\Delta t}{t_i}$ %) over time for (a) VP and (b) BP flake. The solid red lines in (a) and (b) show best fits to experimental data from which slopes (m_{VP} and m_{BP}) were derived. Percent-degraded area (squares) extracted from topographic images and theoretical calculations (red and blue lines) for (c) VP and (d) BP flake. Normalized experimental nano-FTIR amplitude spectra at two different days with respect to the Si substrate for (e) VP and (f) BP flakes, respectively. Normalized second harmonic near-field amplitude values at 1000 cm^{-1} over time for (g) VP and (h) BP flakes.

when compared to VP exposed to the same ambient conditions. In addition to the dramatic increase in height during VP and BP chemical degradation, the surface area of the degraded bubbles in both flakes increases laterally albeit at different rates. We show plots of the measured fraction of the degraded areas as a function of time in Figs. 3(c) and 3(d) for VP and BP flakes, respectively. Each data point on the plots (dark squares) in Figs. 3(c) and 3(d) represents the sum of the measured area of each degraded bubble divided by the total area of the sample. The degraded surface area was measured using the change in the height of a given location on a sample by setting a height threshold value for each scan. The experimental plot shown in Fig. 3(c) reveals that for the VP flake, the degraded area percentage increases steeply with time in the beginning then curves slowly toward saturation and is completely saturated at day 34, at which time, we stopped measuring further height increments in the sample. Like with BP, the degradation of VP begins soon after exfoliation as nano-sized particles appear randomly on the surface; however, the proceeding growth dynamics of the nanoparticles are different from what is

observed in BP, as shown in Fig. 3(d) (also see Ref. 20). In BP, the degraded area percentage change follows the sigmoid (S-shaped) growth curves, where the area percentage of the degraded regions initially increases slowly then grows in an exponential fashion as particles start to coalesce covering the entire surface by day 15.[20,21] The degraded area percentage differences between VP and BP may be explained by different degradation processes as indicated in the phase spectra shown in Fig. 2. To qualitatively understand these differences and the degradation process of VP, we use a variant of the forest-fire model to fit our experimental data. The model is described in detail in Ref. 20; briefly, the sample surface is divided in $N \times N$ square elements, where each square can be either in an undegraded or degraded state. We calculate the degradation probability after a small-time interval Δt using $P_n = 1 - e^{-\Delta t.\eta^{(n)}}$, where $\eta^{(n)}$ is the degradation probability per unit time of a surface element that has n degraded neighbors ($0 \leq n \leq 8$). Each degraded neighbor increases $\eta^{(n)}$ by a fixed amount $\Delta\eta$, that is, $\eta^{(n)} = \eta^{(0)} + n\Delta\eta$, where $\eta^{(0)}$ is the degradation probability per unit time. We note that this model gives a good fit to the VP experimental data only if we neglect the influence of neighbors on the degradation probabilities by setting $\Delta\eta = 0$, as shown by the red curve in Fig. 3(c). If, on the other hand, the influence of degraded neighbors is included, the model does not predict the experimentally observed results [Fig. 3(c) blue curve]. The opposite scenario is true for BP where the model predicts the correct experimental behavior only if the influence of neighbors on the degradation probabilities is included as shown in Fig. 3(d) (also see Ref. 20). The model, thus, suggests, unlike BP, the influence of degraded surface elements on non-degraded ones and does not contribute to the degradation process of VP.

The time-dependent IR near-field amplitude spectra provide information on real-time degradation changes of the real part of the local complex dielectric properties of the sample. Second harmonic normalized nano-FTIR amplitude spectra of VP are shown in Fig. 3(e) taken at the point X in Fig. 2(c) at two different days. A similar plot for BP taken at the point Y in Fig. 2(d) is shown in Fig. 3(f). The normalized amplitude values decrease significantly over time as the samples degrade, which also complements the increasing topographic height in Figs. 3(a) and 3(b). Figures 3(g) and 3(h) show the second harmonic normalized nano-FTIR amplitude spectra values extracted at 1000 cm^{-1} from amplitude spectra for VP and BP, respectively, over time. The decreasing normalized amplitude signal level, shown over several days in Figs. 3(g) and 3(h), is caused by continually decreasing polarizability of the sample during degradation over time, and the effective real-part of the dielectric functions is continuously decreasing for both VP and BP flakes affecting the tip-sample near-field coupling.[14–16]

In summary, we have studied ambient degradation of CVD-synthesized VP in comparison with BP using Raman and nano-FTIR spectroscopy in the frequency range 800–1500 cm^{-1}. VP Raman spectra are characterized by several peaks in the frequency range 100–300 and 350–500 cm^{-1} including stretching and bending modes, angle distortions, and rotational distortions. The nano-FTIR phase spectra of VP and BP show broad peaks on top of a broad background resulting from a combination of many overlapping phosphorus oxides and phosphoric acids species modes in the range of 850–1300 cm^{-1}, which increase in intensity with time due to the degradation of the surface. Differences in the degradation spectra as well as thickness and permittivity changes between VP and BP indicate reduced oxygen insertion in VP, resulting in slower degradation compared to BP. VP is a vdW material with promising electronic and photonic applications, and a fundamental understanding of its properties and degradation process in comparison with other phosphorus allotropes will likely enable the realization of its full technological potential.

A.F. and Y.A. acknowledge support from the Air Force Office of Scientific Research, Grant No. 426 No. FA9559-16-1-0172, and National Science Foundation (CAREER), Grant No. 1553251. M.S. acknowledges support from the Air Force Office of Scientific Research under Award No. FA9550-19RYCOR050.

DATA AVAILABILITY

The data that support the findings of this study are available from the corresponding author upon reasonable request.

REFERENCES

[1]P. W. Bridgman, J. Am. Chem. Soc. **38**(3), 609 (1916).
[2]R. Schuster, J. Trinckauf, C. Habenicht, M. Knupfer, and B. Büchner, Phys. Rev. Lett. **115**(2), 026404 (2015).
[3]H. Liu, Y. Du, Y. Deng, and P. D. Ye, Chem. Soc. Rev. **44**(9), 2732 (2015).
[4]Y. Abate, D. Akinwande, S. Gamage, H. Wang, M. Snure, N. Poudel, and S. B. Cronin, Adv. Mater. **30**(29), 1704749 (2018).
[5]L. Li, Y. Yu, G. J. Ye, Q. Ge, X. Ou, H. Wu, D. Feng, X. H. Chen, and Y. Zhang, Nat. Nanotechnol. **9**(5), 372 (2014).
[6]L. Zhang, H. Huang, B. Zhang, M. Gu, D. Zhao, X. Zhao, L. Li, J. Zhou, K. Wu, Y. Cheng, and J. Zhang, Angew. Chem., Int. Ed. **59**(3), 1074 (2020).
[7]C. Gu, S. Zhao, J. L. Zhang, S. Sun, K. Yuan, Z. Hu, C. Han, Z. Ma, L. Wang, F. Huo, W. Huang, Z. Li, and W. Chen, ACS Nano **11**(5), 4943 (2017).
[8]Y. Zhou, M. Zhang, Z. Guo, L. Miao, S.-T. Han, Z. Wang, X. Zhang, H. Zhang, and Z. Peng, Mater. Horiz. **4**(6), 997 (2017).
[9]J. E. Padilha, A. Fazzio, and A. J. R. da Silva, Phys. Rev. Lett. **114**(6), 066803 (2015).
[10]H. Liu, A. T. Neal, Z. Zhu, Z. Luo, X. Xu, D. Tománek, and P. D. Ye, ACS Nano **8**(4), 4033 (2014).
[11]Z. Zhang, D.-H. Xing, J. Li, and Q. Yan, CrystEngComm **19**(6), 905 (2017).
[12]L. Zhang, M. Gu, L. Li, X. Zhao, C. Fu, T. Liu, X. Xu, Y. Cheng, and J. Zhang, Chem. Mater. **32**(17), 7363 (2020).
[13]G. Fasol, M. Cardona, W. Hönle, and H. G. von Schnering, Solid State Commun. **52**(3), 307 (1984).
[14]F. Huth, A. Govyadinov, S. Amarie, W. Nuansing, F. Keilmann, and R. Hillenbrand, Nano Lett **12**(8), 3973 (2012).
[15]J. M. Stiegler, Y. Abate, A. Cvitkovic, Y. E. Romanyuk, A. J. Huber, S. R. Leone, and R. Hillenbrand, ACS Nano **5**(8), 6494 (2011).
[16]A. Fali, S. Gamage, M. Howard, T. G. Folland, N. A. Mahadik, T. Tiwald, K. Bolotin, J. D. Caldwell, and Y. Abate, ACS Photonics **8**, 175 (2020).
[17]D. E. C. Corbrjdge, J. Appl. Chem. **6**, 456 (1956).
[18]M. Lechs and G. Zundel, Can. J. Chem. **57**, 487 (1979).
[19]J. D. Wood, S. A. Wells, D. Jariwala, K.-S. Chen, E. Cho, V. K. Sangwan, X. Liu, L. J. Lauhon, T. J. Marks, and M. C. Hersam, Nano Lett **14**(12), 6964 (2014).
[20]S. Gamage, Z. Li, V. S. Yakovlev, C. Lewis, H. Wang, S. B. Cronin, and Y. Abate, Adv. Mater. Interfaces **3**(12), 1600121 (2016).
[21]S. Gamage, A. Fali, N. Aghamiri, L. Yang, P. D. Ye, and Y. Abate, Nanotechnology **28**(26), 265201 (2017).